HHS Public Access

Author manuscript

Science. Author manuscript; available in PMC 2016 April 23.

Published in final edited form as:

Science. 2015 October 23; 350(6259): aac5137. doi:10.1126/science.aac5137.

HIV-1 Nef hijacks clathrin coats by stabilizing AP-1:Arf1 polygons

Qing-Tao Shen[1,†], **Xuefeng Ren**[1,†], **Rui Zhang**[2,†], **Il-Hyung Lee**[1], and **James H. Hurley**[1,2,*]

[1]Department of Molecular and Cell Biology and California Institute for Quantitative Biosciences, University of California, Berkeley, Berkeley, CA 94720, USA

[2]Life Sciences Division, Lawrence Berkeley National Laboratory, Berkeley, CA 94720, USA

Abstract

The lentiviruses HIV and SIV subvert intracellular membrane traffic as part of their replication cycle. The lentiviral Nef protein helps viruses evade innate and adaptive immune defenses by hijacking the AP-1 and -2 clathrin adaptors. Here we found that HIV-1 Nef and the GTPase Arf1 induced trimerization and activation of AP-1. We report the cryoelectron microscopy structures of the Nef and Arf1-bound AP-1 trimer in active and inactive states. A central nucleus of three Arf1 molecules organizes the trimers. We combined the open trimer with a known dimer structure, which predicted a hexagonal assembly whose inner and outer faces bind the membranes and clathrin, respectively. Hexagons were directly visualized and the model validated by reconstituting clathrin cage assembly. Arf1 and Nef thus play interconnected roles in allosteric activation, cargo recruitment, and coat assembly, revealing an unexpectedly intricate organization of the inner AP-1 layer of the clathrin coat.

Vesicular coats are involved in intracellular membrane traffic and are central to the organization of eukaryotic cells (1). Coats consist of (*i*) a structural scaffold and (*ii*) adaptor elements that link the scaffold to membrane proteins and lipids. The scaffold and adaptor may exist as separate layers or they may be combined. Clathrin is the archetypal two-layer vesicular coat (2), and is responsible for much of the vesicular traffic originating at the plasma membrane and *trans*-Golgi network (TGN), as well as intraendosomal traffic. The clathrin heavy and light chains comprise the scaffold, whilst the heterotetrameric adaptor protein (AP) complexes are the most prevalent adaptor components for clathrin (3, 4). Clathrin does not bind directly to cargo or membranes. The AP complexes connect cargo and membranes on the one hand to clathrin on the other. The AP-1 complex functions at the TGN, where it is recruited and activated by the small GTPase Arf1 (ADP-ribosylation factor-1) (5, 6). AP-1 consists of the two large subunits β1 and γ, a medium subunit μ1, and a small subunit σ1 (3). The large subunits contain flexibly tethered C-terminal ear domains, and constructs lacking the linkers and ears are referred to as AP cores. AP-1 cargoes contain either tyrosine-based sorting signals, which bind to the C-terminal domain (CTD) of μ1, or dileucine signals, which bind to a site spanning the γ and σ1 subunits (4). The activity of AP

*Correspondence to: James H. Hurley jimhurley@berkeley.edu.
†Co-first author.

complexes is tightly regulated, and in the absence of activation, the cargo binding sites are sequestered in a state known as the locked conformation (7, 8). AP-1 is "unlocked" by Arf1-GTP through an allosteric mechanism coupled to formation of a 2:2 AP-1:Arf1 dimer (9).

Human immunodeficiency virus-1 (HIV-1), HIV-2, and simian immunodeficiency virus (SIV) hijack the clathrin pathway via their accessory proteins negative factor (Nef) and viral protein unique (Vpu) (10, 11). Lentiviral hijacking facilitates viral immune evasion, assembly, and release by downregulating cluster of differentiation 4 (CD4) (12, 13), major histocompatibility complex-I (MHC-I) (14), tetherin (15), and other cell surface receptors and restriction factors. AP-1 mediates the ability of Nef and Vpu proteins to reroute MHC-I and tetherin from the plasma membrane to lysosomes (16, 17). Nef hijacks AP-1 to downregulate MHC-I via the tyrosine motif binding site on μ1-CTD (18), while AP-2 is hijacked to downregulate CD4 via the dileucine binding site on the α-σ2 complex (19, 20). Both Nef binding sites are occluded in the locked conformation (21, 22). Nef subversion of membrane traffic thus requires that AP complexes be unlocked. One report has suggested that Nef can drive membrane localization of AP-1 independent of Arf1 (23), while another found that Nef stabilizes the AP-1 coat only in the presence of Arf1 (24) and a third showed that Arf1 is required for Nef-driven downregulation of MHC-I (25). Arf1, along with the subunits of AP-1 and MHC-I, is one of ~50 Nef-interacting proteins detected in the human proteome (26). We set out to determine whether Nef, in combination with host cargo, could either bypass or amplify the endogenous Arf1-dependent unlocking mechanism.

HIV-1 Nef and Arf1 trimerize AP-1

We fused the cytosolic 21 amino acids of tetherin, which bind tightly to AP-1 (17), to full-length HIV-1 NL4-3 Nef. We co-incubated tetherin-Nef, the AP-1 core (henceforward, "AP-1"), and the GTP-locked and N-terminally truncated Arf1 mutant Q71L (henceforward, "Arf1"). These molecules formed a complex that had a molecular weight of 850 kDa as determined by multi-angle light scattering (MALS) (Fig. 1A, B). This corresponds to three AP-1:Arf1:tetherin-Nef complexes. In contrast, the AP-1 complex alone migrated at a mass corresponding to a single heterotetramer (Fig. 1B). AP-1:Arf1 contained two peaks, with the higher mass peak corresponding to a species whose dimeric crystal structure is known (9) (Fig. 1A). Other combinations of AP-1, Arf1, and Nef in the presence or absence of a physiological cargo peptide (TGN38) or fused to the tail of MHC-I were also tested. These complexes manifested an apparent mixture of monomer, dimer, and trimer, or in the case of MHC-I, a heterogenous mixture of higher-order species (Fig. 1A, Fig. S1).

The AP-1:Arf1:tetherin-Nef trimers appeared to be promising for structural characterization on the basis of their monodispersity. In order to determine if these trimers corresponded to the unlocked conformation, we developed a Förster resonance energy transfer (FRET) reporter for AP-1 unlocking (Fig. 1C, D). In the locked conformation (27), the separation between β1-Glu471 and μ1-Lys333 was 17 Å, whilst the distance increased to 58 Å in both the unlocked (9) and the even more open hyper-unlocked (17) conformations (Fig. 1D). We constructed an AP-1 variant in which all 34 native Cys were replaced by Ala. The mutation β1E471C μ1K333C was generated in the Cys-free context and fluorescently labeled with Cy3 and Cy5. The labeled AP-1 formed the same 850 kDa complex with tetherin-Nef and

Arf1, and the spectra of the labeled AP-1 alone and in complex with tetherin-Nef and Arf1 were compared (Fig. 1C). The spectra indicated a loss of FRET in the presence of tetherin-Nef and Arf1, consistent with unlocking.

CryoEM reconstruction of AP-1:Arf1:tetherin-Nef trimers

Negative stain and cryoelectron microscopy (cryoEM) images were collected for the gel filtration peak corresponding to the 850 kDa complex, and 2D and 3D classifications were carried out (Fig. 2A, Fig. S2–3). The complex consisted of two different types of trimers, with a small proportion of dimers (Fig. 2A, B). Roughly 24% of the population consisted of particles resembling a three-leaf clover, while ~72% corresponded to triangles. The reconstruction of the three-leaf clover-like particles was improved by masking a sub-assembly to yield a 7 Å reconstruction (Fig. 2C, D, Fig. S4, 5, Movie S1). The density was readily interpretable, and it was straightforward to dock into each of the three clover leaves one copy of the hyper-unlocked conformation of AP-1 (17), one copy of Nef in the conformation bound to μ1-CTD (21), and two Arf1 molecules as bound to β1 (henceforward $Arf1^{\beta}$) (9) and to the coatomer (COP-I) counterpart of γ (henceforward $Arf1^{\gamma}$) (28) (Fig. S5). These molecules collectively accounted for essentially all of the density (Fig. 2D, 3A).

Arf^{γ} and $Arf1^{\beta}$ contacted AP-1 via their GTP-responsive switch I and II (SwI/II) regions, consistent with the GTP-dependence of Arf1 activation of AP-1 (Fig. 3B). The region of Arf^{γ} comprising residues His80, Gln83, Glu113, Asp114, and Glu115, outside the SwI/II regions, contacts the tip of the cargo-binding μ1-CTD (Fig. 3C). This part of μ1-CTD moves ~27 Å from its position in the conventional unlocked structure in order to make these contacts. These μ1-CTD contacts with Arf1 presumably help drive the hyper-unlocked conformation in the Arf1-linked trimer. The trimer is held together in part by direct contacts between three copies of $Arf1^{\gamma}$. The region of Asn175 and Arg178, and the C-terminal Lys181 of one Arf1 contact the region of His146-Trp153 and Gln176-Asn179 residues of the next (Fig. 3D). Arf1 is not known to trimerize in isolation, and we surmise that either (*i*) AP-1 promotes a unique conformation of Arf1 that is prone to trimerization, or (*ii*) additional contacts elsewhere in the assembly cooperate to promote the trimer. With respect to (*i*), at 7 Å resolution it is not possible to determine if AP-1 induces subtle conformational changes in Arf1. With respect to (*ii*), a major inter-leaf bridge is made by a contact between the N-termini of Nef and β1 that stabilizes the trimer (Fig. 2D, 3E). The clover-shaped trimer sequesters the cargo-binding site of the three μ1-CTD such that they face the center of the trimer, hence membrane interactions are precluded. Even though the individual AP-1 complexes are in the hyper-unlocked conformation, the overall trimer is closed (Fig. 3F). Thus we refer to this minority population of trimers as “closed” and conclude that this state is inactive for vesicle formation.

The majority population of triangle-shaped particles yielded a 17 Å reconstruction (Fig. 4A, Fig. S6–8, Movie S2). The resolution was limited by heterogeneity in the position of the three monomers within the triangle, which visibly contact one another only in the center. The density can be reasonably explained by docking three copies of the “monomeric” AP-1:$Arf1^{\gamma}$ unit of the closed-state model described above (Fig. 4A). Each AP-1:$Arf1^{\gamma}$ complex was docked as a rigid body, while maintaining the central nucleus of three Arf^{γ}. Due to the

mobility of the monomers, we cannot visualize clear density for Nef or Arf1$^{\beta}$, although Nef is stoichiometrically bound in the sample (Fig. 1A). The C-termini of β1 come into close approach at the center. In this structure, the tyrosine and dileucine binding sites, the myristoylation site at the N-terminus of Arf1, and the PI(4)P binding site of AP-1 fall into an approximate plane (Fig. 4B). Since all of the sites are accessible, we refer to this state as "open".

AP-1:Arf1 hexagonal rings

A previous crystal structure of a 2:2 unlocked AP-1:Arf1 complex solved in the absence of Nef and cargo led to a model for Arf1 activation in the context of a dimeric assembly (9). In that structure, the SwI/II Arf1$^{\beta}$ contact was present, and a second contact was made between Trp172 of the back side of Arf1$^{\beta}$ and the α12-α16 region of γ (Fig. 4C). The mutation W172D prevents Arf1 from activating AP-1, which validated the role of the dimer contact in activation. This posed the question as to the relationship between the previous dimer and the current trimer structure. In the open trimer structure, the Arf1$^{\beta}$ site and γ-α12-α16 are unobstructed and aligned in a plane parallel to the membrane. We docked the dimeric crystal structure onto these sites (Fig. 4C). Iterative docking of dimers and trimer linked by Arf1$^{\beta}$ bridges generated a hexagonal ring consisting of a total of 18 AP-1 complexes and 36 Arf1 molecules (Fig. 4D). The ring is essentially identical in diameter to the hexagons seen in the cryoEM reconstruction of the clathrin cage (29) (Fig. 4E). The clathrin binding sequence of β1 is located directly under the projections of the clathrin density corresponding to the clathrin terminal domain (Fig. 4F). The AP-1:Arf1 hexagon is thus in almost perfect alignment to template the recruitment and organization of clathrin.

Spurred by this model, we revisited the high molecular weight tail of the polydisperse AP-1:Arf1:MHC-I-Nef sample (Fig. 1A, Fig. S9). We had originally considered this material too heterogeneous for EM analysis and had set it aside, even though MHC-I is the best known substrate for HIV-1 Nef downregulation via AP-1. The earliest-eluting fractions of this material were subjected to negative stain EM (Fig. 5A). We observed polygons in abundance whose dimensions were consistent with the mode of oligomerization suggested by the model. These included a substantial population of closed hexagons. In order to quantitate the relative numbers of different particles, we subjected them to 2D class averaging (Fig. 5A). The particles were not perfectly identical and the averages therefore lost density near the edges. Nevertheless, when atomic models were superimposed on the raw images, convincing fits were obtained (Fig. 5B).

Clathrin cage assembly promoted by AP-1 hexagons

In order to validate the Arf1-mediated dimer and trimer interfaces, Arf1 mutants were constructed in the SwI region (I49D) (30), the dimer contact with the back side of Arf1$^{\beta}$ (W172D) (9), and the two regions involved in the central trimer contacts (Fig. 5C). All of these mutants were stable and purified in isolation as monomers (Fig. S10). We then tested their ability to oligomerize in the context of the AP-1:Arf1:unfused Nef complex. The wild-type complex runs as a mixture of trimer and higher-order species (Fig. 5D). No isolated dimeric species was seen in the size-exclusion chromatography of this complex, but the

higher order species were presumed to arise via a combination of dimer and trimer interactions. The dimer interface mutant W172D yields a sharper trimer peak and reduces the proportion of higher-order species (Fig. 5D). The SwI mutant I49D and the trimer-interface loop replacement Arf1$^{\Delta 148\text{-}152GS}$ completely eliminate both the trimer and larger species. The C-terminal deletion Arf1$^{\Delta 178\text{-}181}$ reduces but does not eliminate the trimer. These findings are all consistent with the observed set of structural contacts.

We went on to reconstitute clathrin cages in vitro (Fig. 5E) in order to determine whether formation of Nef- and Arf1-promoted polygons in turn promoted clathrin assembly. Wild-type Arf1 and Nef supported efficient cage assembly (Fig. 5F). In contrast, the SwI, dimer, and one of the trimer interface mutants had near-background levels of cage assembly (Fig. 5F). The second trimer interface mutant, the deletion of the C-terminal four residues, had a modest effect of borderline significance (Fig. 5F). The limited effect of this mutant is consistent with the modest reduction in the trimer peak seen in Fig. 5D. Thus the Arf1 bridges that hold the dimer and trimer together are essential for promotion of clathrin cage assembly.

We mutated key residues in Nef contacts with AP-1 to probe their role in activating clathrin cage formation. Nef is capable of binding to the γ-σ1 hemicomplex of AP-1 via its dileucine motif (31) (Fig. 6A). The dileucine-γ-σ1 interaction is not essential for downregulation of MHC-I by AP-1, and Nef is not visualized at this site in the EM density. Nevertheless, we reasoned that wild-type Nef can still bind to this site and could promote unlocking. We tested the ability of Nef$^{LL164\text{-}165AA}$ and MHC-I-Nef$^{LL164\text{-}165AA}$ to promote AP-1 oligomerization and clathrin cage assembly. In the presence of Nef$^{LL164\text{-}165AA}$, AP-1 and Arf1 migrated as if Nef were absent (Fig. 6B), and clathrin cage assembly was reduced to the same background level seen without Nef (Fig. 6C). MHC-I and tetherin cooperate with Nef to bind to μ1-CTD via an interface that does not involve the dileucine motif, but does involve Asp123 (21). This is the site that is well-ordered in the EM density of the closed trimer in the presence of cargo. MHC-I-Nef$^{LL164\text{-}165AA}$ still trimerizes AP-1 (Fig. 6D), although the presence of higher-order oligomers was reduced. MHC-I-Nef$^{LL164\text{-}165AA}$ promotes clathrin cage assembly (Fig. 6E) with efficiency relatively near wild-type, consistent with the biological finding that MHC-I downregulation does not require the dileucine motif (32). Conversely, MHC-I-Nef^{D123R}, which destabilizes the μ1-CTD interface, reduced the proportion of trimeric AP-1 (Fig. 6D) and reduced clathrin cage assembly to about 30% of wild-type (Fig. 6E). In the absence of MHC-I, Nef^{D123R} had essentially wild-type oligomerization (Fig. 6B) and cage assembly behavior (Fig. 6C), consistent with the dependence of the Nef-μ1-CTD interaction on the presence of μ1-CTD-directed cargo (21).

Conclusions

Previous models of AP-mediated clathrin recruitment have focused on the plasma membrane adaptor AP-2, which is activated principally by PI(4,5)P_2, not Arf1 (33). In the reconstruction of an AP-2-clathrin coat, the AP-2 complexes were disordered and substoichiometric (29). The recruitment of clathrin to the plasma membrane appears to be coupled to recruitment of pairs of AP-2 complexes (34), rather than a larger scaffold. Our

contrasting findings of an ordered inner layer for AP-1 point to a fundamental difference between the AP-1 and AP-2 coats. These findings for AP-1 do seem likely to apply also to the Arf1-activated AP-3 adaptor complex. A very recent cryoEM tomographic study of COP-I vesicles (35) noted similar Arf1-mediated trimers to those seen here. In other ways, the two layer hexagonal organization described here for AP-1 and clathrin differs from the interwoven assembly of COP-I. In summary, the results show that the inner layer of the AP-1-clathrin coat, and probably other Arf1-dependent clathrin coats, has a far more organized structure than previously appreciated. Moreover, Arf1 plays a far more central role than previously understood. Not only does Arf1 drive recruitment and allosteric activation of AP-1, we have now found that it is an integral component of the structure of the inner layer, bridging the individual AP-1 complexes into dimers and trimers and thence to 18-mer hexagons.

The highly organized inner layer structure introduces an additional level at which regulation can occur. HIV-1 Nef appears to take advantage of the additional complexity by promoting trimer formation, which could allow it to template clathrin cages under conditions that would otherwise fall short of full activation (Fig. 6F). Trimer promotion appears to occur by both indirect and direct mechanisms. The structural observation that Nef can bridge between different AP-1 complexes within the trimer suggests that Nef can also drive trimerization directly. The loss of function for $Nef^{LL164\text{-}165AA}$ in the absence of MHC-I is consistent with an indirect mechanism, wherein Nef binds tightly to γ-σ1 (31), driving the thermodynamic equilibrium towards the unlocked state, which in turn is capable of trimerizing. We currently believe these two mechanisms can work either alone or together in different contexts.

MHC-I-Nef is much more effective than tetherin-Nef at promoting polygon formation, even though both constructs bind tightly to AP-1. HIV-1 NL4-3 (the source of Nef used in this study, and a member of group M) downregulates MHC-1 via Nef, and tetherin via Vpu. However, HIV group O, like simian immunodeficiency virus (SIV), uses Nef to downregulate tetherin (36). Perhaps HIV-1 O-Nef and SIV Nef might be more effective the HIV-1 NL4-3 or other M- and N-Nefs at promoting polygon formation in the presence of tetherin. If confirmed, this would provide a molecular mechanism for virus-specific differences in the mode of tetherin downregulation.

Our observations of the ordered inner layer of the AP-1 clathrin coat were made in the stabilizing presence of HIV-1 Nef and cargo. The conservation of the Arf1-binding sites in the evolution of AP-1 from yeast to humans leaves little doubt the ordered inner layer is far more ancient than the appearance of the primate lentiviruses. The elaborate organization of the AP-1:Arf1 inner layer might offer advantages to the cell in terms of the speed of clathrin assembly, regulatory versatility, or both. Clathrin coats can be generated on synaptic endosomes within a span of 2 s (37), a pathway that most likely involves the Arf1-activated AP-1 and/or AP-3 complexes. Cooperative assembly of a symmetry-matched hexagonal inner layer would be a clear asset in catalyzing the rapid nucleation of an endosomal clathrin coat. These benefits must have been adaptive early in the evolution of eukaryotes.

Materials and Methods

Plasmid construction

The His_6- and GST-tagged AP-1 core expression construct was described by Ren et al. (9). In variant FLβ.AP-1 complex used for clathrin assembly experiments, β1 (1-584) was replaced with full-length β1 DNA. A tobacco etch virus (TEV) cleavage site and His_6 tag were fused to the C-terminal of full-length β1. To generate the Cys-free construct, DNAs encoding the AP-1 core subunits were codon optimized and synthesized (Genescript, Piscataway, NJ) to generate a Cys-free (C2A) construct, which was then used as a template for site-directed mutagenesis to produce the desired Cys pair construct. HIV-1 NL4-3 Nef, tetherin (1-21)-10 aa linker-Nef and MHC-I (338-365)-Nef were expressed as TEV-cleavable N-terminal His_6 fusions. His_6-tagged full-length Nef was used for clathrin cage assembly. The N-terminal truncation of Nef (56-206) was used for size exclusion chromatography of AP1:Arf1:Nef trimer complexes. Human Arf1 (17-181) Q71L or other Arf1 mutants made in this background were expressed with a TEV-cleavable N-terminal His_6 tag.

Protein expression and purification

The AP-1 complexes were expressed in BL21 (DE3) star (Life technologies, Grand Island, NY) or BL21 (DE3) pLysS strain (Promega, Madison, WI), and induced with 0.3 mM IPTG at 20 °C overnight. The cells were lysed by sonication in 50 mM Tris pH 8.0, 300 mM NaCl, 10% glycerol, 3 mM β-mercaptoethanol (β-ME), and a protease inhibitor cocktail (Sigma-Aldrich, St. Louis, MO). The clarified lysate was first purified on a Ni-NTA column (Qiagen, Valencia, CA). The eluate was further purified on glutathione-Sepharose 4B resin (GE healthcare, Piscataway, NJ). After TEV cleavage at 4 °C overnight, the sample was concentrated and then loaded onto a HiLoad 16/60 Superdex 200 column (GE healthcare) in 20 mM Tris pH 8.0, 200 mM NaCl, 0.3 mM tris(2-carboxyethyl)phosphine (TCEP). The sample fractions were pooled together, adjusted to 30 mM imidazole, and passed through 1 ml of glutathione-Sepharose 4B and then onto a Ni-NTA column (Qiagen) to capture the residual GST and His-tag fragments. The sample was adjusted to 20 mM Tris pH 8.0, 200 mM NaCl, 0.3 mM TCEP by buffer exchange in the concentrator.

His_6-tagged tetherin-Nef and other Nef constructs were expressed in BL21 (DE3) star cells, and induced with 0.3 mM IPTG at 20 °C overnight. The purification was carried out using Ni-NTA resin, and the eluate was subjected to a HiLoad 16/60 Superdex 200 column in the sample buffer. His_6-tagged Arf1 constructs were expressed in BL21 (DE3) star cells by induction at 20°C overnight. The cell pellet was lysed by sonication and purified on a Ni-NTA column in 50 mM Tris pH 8.0, 300 mM NaCl, 20 mM imidazole, 5 mM $MgCl_2$, 3 mM β-ME and a protease inhibitor cocktail. The proteins were eluted with 100 mM imidazole, then loaded onto a HiLoad 16/60 Superdex 75 column (GE healthcare) in sample buffer containing 5 mM $MgCl_2$. Proteins were quantified by the bicinchoninic acid assay (BCA; Pierce) using bovine serum albumin as a standard.

For clathrin purification, a bovine brain was homogenized using a Waring blender in 500 mM Tris pH 7.0, 2 mM EDTA, 3 mM β-ME. The clarified lysate was precipitated at 10%

saturated ammonium sulfate. The pellet was resuspended in 500 mM Tris pH 7.0, 2 mM EDTA, 3 mM β-ME, dialyzed against 30 mM Tris pH 8.5, 2 mM EDTA overnight at 4°C. The dialyzed sample was purified through a monoQ 5/50GL column (GE healthcare), and the clathrin fractions were eluted in 28–35 mS/cm of NaCl concentration. The sample was pooled together and then loaded onto a Superose6 10/100GL column in 30 mM Tris pH 8.0.

Size Exclusion Chromatography with Multiangle Light Scattering (SEC-MALS)

AP-1 core was incubated with Arf1 and tetherin-Nef at 4 °C overnight in 20 mM Tris, pH 8.0, 200 mM NaCl, 0.3 mM TCEP, 5 mM $MgCl_2$, and 1 mM GTP. The molar ratio of AP-1 core: Arf1 (17-181) Q71L: tetherin-Nef was fixed at 1:4:6. The final concentration of AP-1 core was 4 mg/ml (20 μM). SEC-MALS experiments were performed using an Agilent 1200 HPLC system (Agilent Technologies, Santa Clara, CA), coupled to a Wyatt DAWN HELEOS-II MALS instrument and a Wyatt Optilab rEX differential refractometer (Wyatt, Santa Barbara, CA). For chromatographic separation, a WTC-050S5 size-exclusion column (Wyatt) with a 20 μl sample loop was used at a flow rate of 0.3 ml/min in the buffer of 1x PBS, pH 7.4, 5 mM $MgCl_2$, 0.2 mM TCEP. The outputs were analyzed by the ASTRA V software (Wyatt). MALS signals, combined with the protein concentration determined by refractive index, were used to calculate the molecular mass of AP-1:Arf1:tetherin-Nef complex and AP-1 alone.

AP-1:Arf1:Nef complex assembly for EM

Recombinant AP-1 core was mixed with Arf1 and Nef or tetherin-Nef proteins at a molar ratio of 1:4:6, then incubated with 1 mM GTP at 4°C overnight. The mixture was then subjected to a Superose 6 10/100GL column in 20 mM Tris pH 8.0, 200 mM NaCl, 5 mM $MgCl_2$, 0.3 mM TCEP.

Clathrin cage assembly

The total volume of each reaction was 30 μl in HKM buffer (25 mM HEPES pH 7.2, 125 mM potassium acetate, 2 mM $MgCl_2$, 1 mM GppCp (Jena Bioscience, Germany)). His_6-tagged Arf1 (17-181) Q71L proteins (final 0.4 μM) were incubated at 37 °C for 15 min for GTP loading. The mixture was further supplemented with FLβ.AP-1 (final 0.1 μM) and His-Nef or His-MHC-I-Nef (final 0.4 μM) on ice for 15 min. At the last step, clathrin was added into the mixture at the final concentration of 0.3 μM on ice for 15 min, then warmed to 37° C for 15min.

Fluorescent dye labeling

The AP-1 core double cysteine mutant 34Cys-Ala β1E471C μ1K333C was purified and labeled with Cy3 and Cy5 through the simultaneously incubation of $AP\text{-}1^{34CA\beta1E471C\ \mu1K333C}$ (20 μM) with an 8-fold molar excess of Cy3-maleimide and a 10-fold excess of Cy5-maleimide. After overnight incubation at 4°C, unreacted materials were removed on a HiTrap desalting column (GE Healthcare, USA). The final concentration and labeling efficiency were determined by Nanodrop (Thermo scientific) measurement and the BCA protein concentration assay (Pierce). For Arf1:tetherin-Nef complex formation, the

mutant AP-1 was diluted with a 50-fold excess of wild-type AP-1. Incubation and purification condition was identical to other experiments.

Bulk FRET assay

A Fluorolog spectrofluorometer (Horiba, Kyoto, Japan) was used for bulk FRET measurements. Micro square open top fluorometer cells (Starna cells, CA, USA) were used to contain samples. Emission spectra of samples were obtained by scanning emission wavelength from 600 nm to 900 nm with a 532 nm excitation wavelength. A 5 nm slit width was used. The same emission wavelength scan with 640 nm excitation was also performed to estimate the total amount of Cy5. We summed emission counts from 660–664 nm to normalize the 532 nm excitation spectrum to facilitate comparison between spectra.

Negative stain electron microscopy

AP-1 core, Arf1, Nef, tetherin-Nef, MHC-I-Nef and their derivatives at different conditions were adjusted to total protein concentrations of 0.02 mg/ml for negative stain EM. 4 μl droplets of sample were placed on glow-discharged carbon coated copper grids and negatively stained using 2% (w/v) uranyl acetate. For clathrin-related samples, we allowed an extra 5 min incubation time on the grid with 3% glutaraldehyde to fix clathrin cages prior to the application of uranyl acetate, as described before with minor modifications (38). Negatively stained samples were examined under a Tecnai F20 microscope (FEI, Netherlands) operated at an accelerating voltage of 120 keV with a defocus from −1.0 to −1.5 μm at tilts of 0° or 45°. Micrographs were recorded on a charge-coupled device camera (Ultrascan 4000, 4 k × 4k; Gatan) at a nominal magnification of 80,000× with a 1.37 Å calibrated pixel size at the specimen level using the semi-automated Leginon data collection software (39).

Cryoelectron microscopy

Droplets of 2.5 μl AP-1, Arf1 and tetherin-Nef complex sample at a concentration of 0.06 mg/ml were applied to Quantifoil grids with continuous carbon support and plunge frozen into liquid ethane using a Vitrobot Mark IV (FEI, Netherlands). The vitrified samples were examined using a Titan microscope (FEI, Netherlands) operated at 300 keV. The vitrified samples were imaged under parallel illumination conditions, with a beam diameter of ~2 mm on the specimens and a defocus range from −1.5 to −3.5 μm. All cryoEM images were recorded on a K2 Summit direct electron detector camera (Gatan, CA, USA) at a nominal magnification of 27,500×, corresponding to a calibrated pixel size of 1.32 Å. The camera was operated in counting mode, with a dose rate of ~8 electrons/pixel/second on the camera. A total exposure time of 10 s, corresponding to an accumulated dose of 45.9 electrons/$Å^2$ on the specimen, was fractionated into 25 movie frames, with 0.4 s exposure time and a dose of 1.84 electron/$Å^2$ for each frame. The data were collected semi-automatically using the Leginon data collection software (39). Drift correction for movie frames was performed using the UCSF motioncorr program (40). The parameters of the contrast transfer function (CTF) were estimated from the drift-corrected micrographs using CTFFIND4 (http://grigoriefflab.janelia).

Image Processing

The program XMIPP/3.1 was used for 2D analysis and random conical tilt (RCT) analysis of negatively stained samples (41). A total of 11,589 untilted and tilted particle pairs were manually selected from 176 micrograph pairs. The untilted image stack was subjected to reference-free two-dimensional (2D) classification (50 classes) (42). For 38 representative classes, the corresponding tilted particle images were used to compute 3D reconstructions using the RCT approach (43). The obtained 3D reconstructions were classified into 3 groups by visual inspection (open triangles, closed three-leaf clover and dimer-like). Both untilted and tilted particles belonging to each trimeric shape were combined and used to generate a final structure based on projection match. The final resolutions for the open trimer and closed trimer were determined as 27 Å and 26 Å, respectively, based on the 0.5 criterion of the Fourier shell correlation (FSC).

Further cryoEM data analysis of images obtained from the Titan microscope were all performed using RELION/1.4-beta-1 (44). Particles were picked from 1445 drift-corrected micrographs using DoG-Picker (45) inside the APPION image processing suite (46), and the particle coordinates were transferred to RELION for particle extraction. A total of 144,261 individual particles were subject to reference-free 2D classification (using 100 classes) to remove poor quality particles. The remaining dataset comprising 111,183 particles was used for further analyses. Using the RCT structure low-pass filtered to 60 Å as an initial model, we performed 3D classification with 10 classes, which after 50 iterations revealed two major conformations, closed (one class) and open trimers (eight classes). Further 3D classification of the closed class (26,069 particles) into 5 subclasses revealed that the third subunit is wobbling with respect to the rest two subunits (Figure S5D). The flexibility of the third subunit limited the refinement resolution of the whole trimer to 9.0 Å. In order to improve the resolution of the round-edge class, we masked away the third subunit during the auto-refinement and produced a reconstruction for the two rigid subunits at 8.1 Å. A similar strategy to mask out only one subunit from the trimer during the auto-refinement further improved the resolution to 7.0 Å. The other eight open-state classes were re-classified into four classes and 32,535 particles were selected for subsequent auto-refinement process. Due to the sample heterogeneity, the refinement was limited to 23.8 Å resolution. Considering that all classes superimpose reasonably well with respect to each other and revealed an apparent C3 symmetry, at least at low-to-medium resolution. Therefore, we enforced C3 symmetry during the refinement, which resulted in a final resolution of 16.7 Å. All reported resolutions for the RELION reconstruction are based on the gold standard 0.143 FSC criterion using two independent half-maps, with the effects from the soft-edged mask corrected. The angular distribution of each structures was also performed in RELION package.

Docking and Structural Analysis

Crystal structures of the hyper-unlocked AP-1 core bound to tetherin (PDB ID 4P6Z) (17), unlocked AP-1 core with Arf1 (PDB ID 4HMY) (9) and closed AP-1 core (PDB ID 1W63) (27) were used as trial structures for docking. The docking was fulfilled in UCSF Chimera based on rigid-body docking strategy (47). In closed trimer, the crystal structure of hyper-unlocked AP-1 fitted well into the EM density map as an intact unit. Most of the α-helices

of the β and γ subunits in AP-1 were clearly visualized in the density, and β-sandwich of the μ1 subunit also fit well in the density. Besides densities occupied by AP-1 core, two of the three unassigned EM densities were identified to be Arf1 (PDB ID 1O3Y) (48), based on excellent matching of α-helices with the EM densities. The third unoccupied EM density lies close to μ1 domain and was docked well using Nef (PDB ID 4EMZ), which is further verified by the known interface between AP-1:Arf1:Nef (9) and the solved structure of the μ1 domain, Nef, and MHC-I (21). The hyper-unlocked AP-1 with $Arf1^{\gamma}$ was fitted into the EM density map for the open trimer, with or without C3 symmetry, as an intact unit. Preliminary docking results were selected from 500 random placements with the best cross-correlation values and most hits. The possible candidates were further screened based on both symmetrized C3 docking and the position of $Arf1^{\gamma}$ in the EM density.

Supplementary Material

Refer to Web version on PubMed Central for supplementary material.

Acknowledgments

We thank E. Nogales for suggestions and advice, J. Bonifacino for discussions, S. Wu, Y. Cheng, and B. LaFrance for assistance at the outset of the project, and A. Johnson for assistance with figure preparation. This work was supported by the HARC collaborative fund (J. H.H.; subaward of NIH grant P50GM082250 to A. Frankel) and by NIH grant R01AI120691 (J.H.H). Electron microscopy facilities were supported by the Howard Hughes Medical Institute (E. Nogales). All EM maps have been deposited in the Electron Microscopy Data Bank (accession code: EMD-6385 for closed trimer, EMD-6388 for closed monomer, EMD-6389 for open trimer).

References and Notes

1. Schekman R, Orci L. Coat proteins and vesicle budding. Science. 1996; 271:1526. [PubMed: 8599108]
2. Kirchhausen T, Clathrin. Annu Rev Biochem. 2000; 69:699. [PubMed: 10966473]
3. Owen D, Collins B, Evans P. Adaptors for clathrin coats: structure and function. Annu Rev Cell Dev Biol. 2004; 20:153. [PubMed: 15473838]
4. Traub LM, Bonifacino JS. Cargo Recognition in Clathrin-Mediated Endocytosis. Cold Spring Harbor Perspectives in Biology. 2013; 5
5. Stamnes MA, Rothman JE. The binding of AP-1 clathrin adaptor particles to Golgi membranes requires ADP-ribosylation factor, a small GTP-binding protein. Cell. 1993; 73:999. [PubMed: 8500185]
6. Traub LM, Ostrom JA, Kornfeld S. Biochemical dissection of AP-1 recruitment onto Golgi membranes. J Cell Biol. 1993; 123:561. [PubMed: 8227126]
7. Jackson L, et al. A large-scale conformational change couples membrane recruitment to cargo binding in the AP2 clathrin adaptor complex. Cell. 2010; 141:1220. [PubMed: 20603002]
8. Canagarajah B, Ren X, Bonifacino JS, Hurley JH. The clathrin adaptor complexes as a paradigm for membrane-associated allostery. Protein Sci. 2013; 22:517. [PubMed: 23424177]
9. Ren X, Farias GG, Canagarajah B, Bonifacino JS, Hurley JH. Structural Basis for Recruitment and Activation of the AP-1 Clathrin Adaptor Complex by Arf1. Cell. 2013; 152:755. [PubMed: 23415225]
10. Malim MH, Emerman M. HIV-1 accessory proteins - Ensuring viral survival in a hostile environment. Cell Host Microbe. 2008; 3:388. [PubMed: 18541215]
11. Collins DR, Collins KL. HIV-1 Accessory Proteins Adapt Cellular Adaptors to Facilitate Immune Evasion. PLoS Path. 2014; 10
12. Garcia J, Miller A. Serine phosphorylation-independent downregulation of cell-surface CD4 by nef. Nature. 1991; 350:508. [PubMed: 2014052]

13. Aiken C, Konner J, Landau N, Lenburg M, Trono D. Nef induces CD4 endocytosis: requirement for a critical dileucine motif in the membrane-proximal CD4 cytoplasmic domain. Cell. 1994; 76:853. [PubMed: 8124721]
14. Schwartz O, Marechal V, Le Gall S, Lemonnier F, Heard JM. Endocytosis of major histocompatibility complex class I molecules is induced by the HIV-1 Nef protein. Nat Med. 1996; 2:338. [PubMed: 8612235]
15. Neil SJD, Zang T, Bieniasz PD. Tetherin inhibits retrovirus release and is antagonized by HIV-1 Vpu. Nature. 2008; 451:425. [PubMed: 18200009]
16. Roeth JF, Williams M, Kasper MR, Filzen TM, Collins KL. HIV-1 Nef disrupts MHC-1 trafficking by recruiting AP-1 to the MHC-1 cytoplasmic tail. J Cell Biol. 2004; 167:903. [PubMed: 15569716]
17. Jia X, et al. Structural basis of HIV-1 Vpu-mediated BST2 antagonism via hijacking of the clathrin adaptor protein complex 1. Elife. 2014; 3
18. Le Gall S, et al. Nef interacts with the mu subunit of clathrin adaptor complexes and reveals a cryptic sorting signal in MHC I molecules. Immunity. 1998; 8:483. [PubMed: 9586638]
19. Chaudhuri R, Lindwasser O, Smith W, Hurley J, Bonifacino J. Downregulation of CD4 by human immunodeficiency virus type 1 Nef is dependent on clathrin and involves direct interaction of Nef with the AP2 clathrin adaptor. J Virol. 2007; 81:3877. [PubMed: 17267500]
20. Doray B, Lee I, Knisely J, Bu G, Kornfeld S. The gamma/sigma1 and alpha/sigma2 hemicomplexes of clathrin adaptors AP-1 and AP-2 harbor the dileucine recognition site. Mol Biol Cell. 2007; 18:1887. [PubMed: 17360967]
21. Jia X, et al. Structural basis of evasion of cellular adaptive immunity by HIV-1 Nef. Nat Struct Mol Biol. 2012; 19:701. [PubMed: 22705789]
22. Ren X, Park SY, Bonifacino JS, Hurley JH. How HIV-1 Nef hijacks the AP-2 clathrin adaptor to downregulate CD4. eLife. 2014; 3:e01754. [PubMed: 24473078]
23. Janvier K, et al. HIV-1 Nef stabilizes the association of adaptor protein complexes with membranes. J Biol Chem. 2003; 278:8725. [PubMed: 12486136]
24. Coleman SH, Hitchin D, Noviello CM, Guatelli JC. HIV-1 Nef stabilizes AP-1 on membranes without inducing ARF1-independent de novo attachment. Virology. 2006; 345:148. [PubMed: 16253302]
25. Wonderlich ER, et al. ADP Ribosylation Factor 1 Activity Is Required To Recruit AP-1 to the Major Histocompatibility Complex Class I (MHC-I) Cytoplasmic Tail and Disrupt MHC-I Trafficking in HIV-1-Infected Primary T Cells. J Virol. 2011; 85:12216. [PubMed: 21917951]
26. Jaeger S, et al. Global landscape of HIV-human protein complexes. Nature. 2011; 481:365. [PubMed: 22190034]
27. Heldwein EE, et al. Crystal structure of the clathrin adaptor protein 1 core. Proc Natl Acad Sci U S A. 2004; 101:14108. [PubMed: 15377783]
28. Yu XC, Breitman M, Goldberg J. A Structure-Based Mechanism for Arf1-Dependent Recruitment of Coatomer to Membranes. Cell. 2012; 148:530. [PubMed: 22304919]
29. Fotin A, et al. Molecular model for a complete clathrin lattice from electron cryomicroscopy. Nature. 2004; 432:573. [PubMed: 15502812]
30. Cherfils J. Arf GTPases and their effectors: assembling multivalent membrane-binding platforms. Curr Opin Struct Biol. 2014; 29:67. [PubMed: 25460270]
31. Janvier K, et al. Recognition of dileucine-based sorting signals from HIV-1 Nef and LIMP-II by the AP-1 gamma-sigma1 and AP-3 delta-sigma3 hemicomplexes. J Cell Biol. 2003; 163:1281. [PubMed: 14691137]
32. Riggs NL, Craig HM, Pandori MW, Guatelli JC. The dileucine-based sorting motif in HIV-1 Nef is not required for down-regulation of class I MHC. Virology. 1999; 258:203. [PubMed: 10366557]
33. Robinson MS, Bonifacino JS. Adaptor-related proteins. Curr Opin Cell Biol. 2001; 13:444. [PubMed: 11454451]
34. Cocucci E, Aguet F, Boulant S, Kirchhausen T. The First Five Seconds in the Life of a Clathrin-Coated Pit. Cell. 2012; 150:495. [PubMed: 22863004]

35. Dodonova SO, et al. A structure of the COPI coat and the role of coat proteins in membrane vesicles assembly. Science. 2015; 349:195. [PubMed: 26160949]
36. Kluge SF, et al. Nef Proteins of Epidemic HIV-1 Group O Strains Antagonize Human Tetherin. Cell Host Microbe. 2014; 16:639. [PubMed: 25525794]
37. Watanabe S, et al. Clathrin regenerates synaptic vesicles from endosomes. Nature. 2014; 515:228. [PubMed: 25296249]
38. Kelly BT, et al. AP2 controls clathrin polymerization with a membrane-activated switch. Science. 2014; 345:459. [PubMed: 25061211]
39. Suloway C, et al. Automated molecular microscopy: the new Leginon system. Journal of Structural Biology. 2005; 151:41. [PubMed: 15890530]
40. Li XM, et al. Electron counting and beam-induced motion correction enable near-atomic-resolution single-particle cryo-EM. Nat Methods. 2013; 10:584. [PubMed: 23644547]
41. Scheres SHW, Nunez-Ramirez R, Sorzano COS, Maria Carazo J, Marabini R. Image processing for electron microscopy single-particle analysis using XMIPP. Nature Protocols. 2008; 3:977. [PubMed: 18536645]
42. Scheres SHW, et al. Maximum-likelihood multi-reference refinement for electron microscopy images. J Mol Biol. 2005; 348:139. [PubMed: 15808859]
43. Radermacher M, Wagenknecht T, Verschoor A, Frank J. 3-Dimensional Reconstruction from a Single-Exposure, Random Conical Titl Series Applied to the 50S-Ribosomal Subunit of Escherichia coli. Journal of Microscopy-Oxford. 1987; 146:113.
44. Scheres SHW. RELION: Implementation of a Bayesian approach to cryo-EM structure determination. Journal of Structural Biology. 2012; 180:519. [PubMed: 23000701]
45. Voss NR, Yoshioka CK, Radermacher M, Potter CS, Carragher B. DoG Picker and TiltPicker: Software tools to facilitate particle selection in single particle electron microscopy. Journal of Structural Biology. 2009; 166:205. [PubMed: 19374019]
46. Lander GC, et al. Appion: an integrated, database-driven pipeline to facilitate EM image processing. 2009
47. Pettersen EF, et al. UCSF chimera - A visualization system for exploratory research and analysis. J Comput Chem. 2004; 25:1605. [PubMed: 15264254]
48. Shiba T, et al. Molecular mechanism of membrane recruitment of GGA by ARF in lysosomal protein transport. Nat Struct Biol. 2003; 10:386. [PubMed: 12679809]

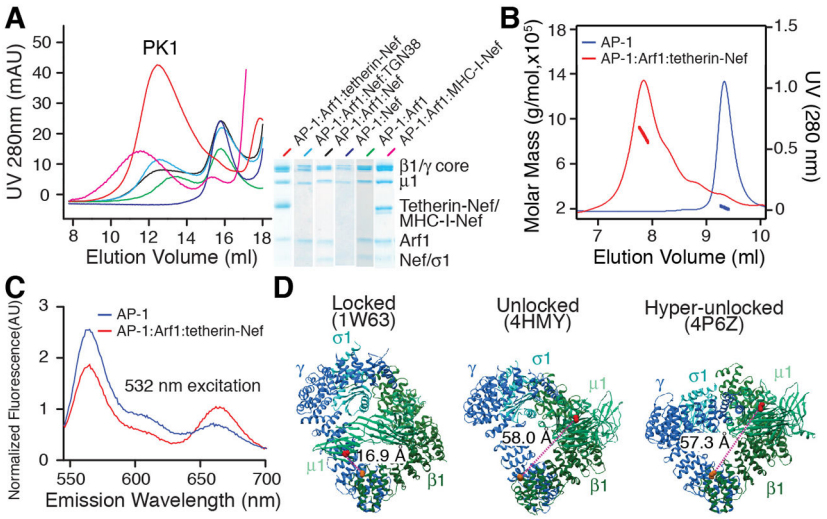

Fig. 1.

Arf1, cargo, and Nef trimerize and unlock AP-1. (**A**) Size exclusion chromatography of AP-1 complexes with the partners indicated with color codes at right. Peak 1 “PK1” indicates the high molecular weight AP-1:Arf1:tetherin-Nef, whose central fraction was used for subsequent biophysical and cryoEM studies. The gel shown at right was loaded with samples from PK1 for AP-1:Arf1:tetherin-Nef, and the highest molecular weight peak eluted for each of the other samples tested. (**B**) Multi-angle light scattering (MALS) of AP-1:Arf1:tetherin-Nef (red), and free AP-1 (blue). (**C**) Emission spectra of free AP-1 and the complex with AP-1:Arf1:tetherin-Nef, with excitation at 532 nm. The increase in Cy3 emission and decrease of Cy5 emission shows the FRET efficiency decreases in the complex. The original intensity counts were normalized by the estimation of total Cy5 amount. (**D**) Distance changes anticipated between the locked and unlocked AP-1 complexes, obtained from the indicated PDB entries. The distance increase from 17 to 58 Å corresponds to a two-fold decrease in FRET efficiency difference for the Cy3-Cy5 pair (R_0^6=60 Å) and $E=R_0^6/(R_0^6+R^6)$.

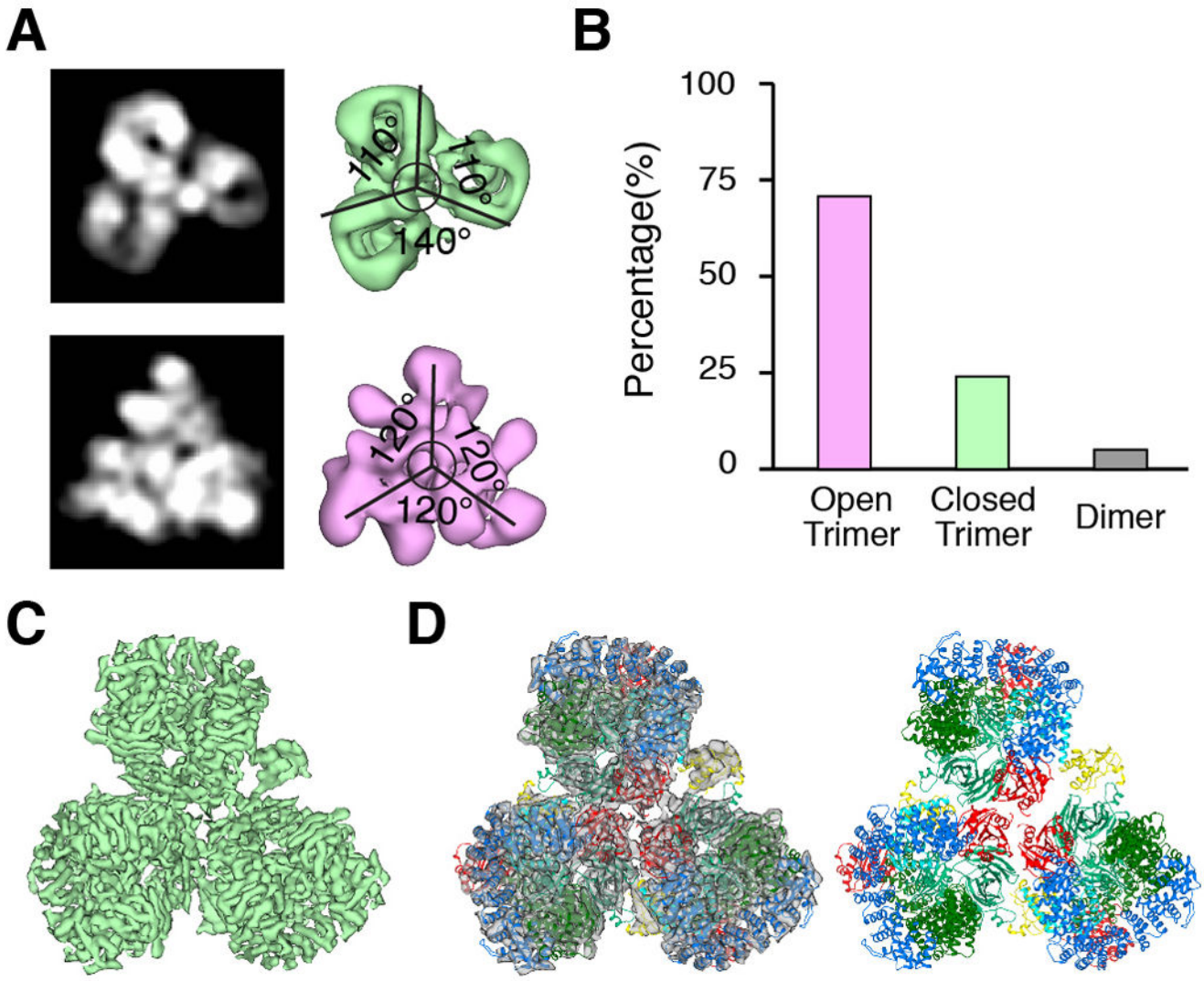

Fig. 2.

CryoEM reconstruction of two types of AP-1:Arf1:tetherin-Nef trimers. (**A**) Representative 2D/3D classes of trimers. (**B**) Relative population of dimers and closed and open trimers. (**C**) Submasking and 7 Å reconstruction of a subassembly of the closed trimer. (**D**) Overall view of the docking of hyper-unlocked AP-1 structure, Arf1, and Nef into closed trimer reconstruction.

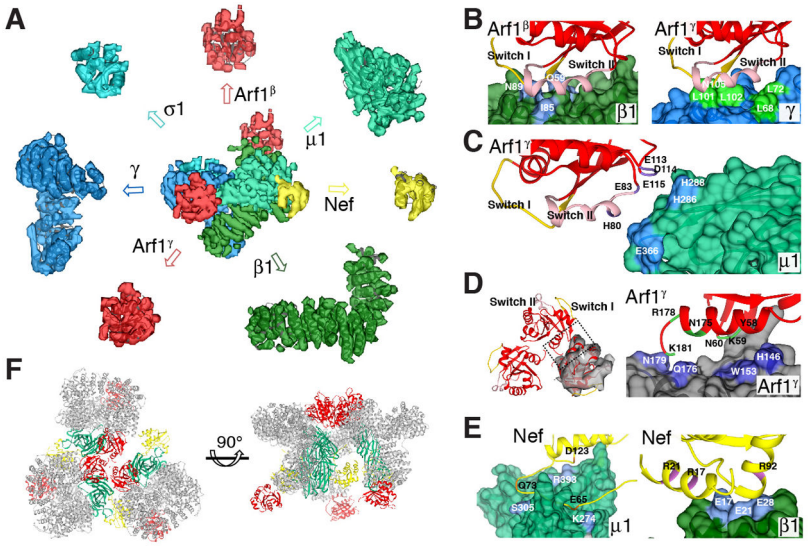

Fig. 3.

Molecular interactions in the closed AP-1:Arf1:tetherin-Nef trimer. (**A**) Exploded view of subunit-by-subunit fits into the closed trimer reconstruction. (**B**) Details of interactions between Arf1 and β1 and γ subunits. (**C**) Interactions between Arf1 and μ1 CTD drive hyper-unlocking. (**D**) Interactions at the center of the Arf1 nucleus stabilize the trimer. (**E**) Interactions between Nef and the μ1-CTD (left) mirror those seen previously (21), while a distinct trimer-bridging interaction is observed between Nef and the N-terminus of β1(right). (**F**) The closed AP-1:Arf1:tetherin-Nef trimer. The reported membrane and cargo binding subunits including Arf1, μ1 and Nef are kept in their original colors, while the other parts are colored grey.

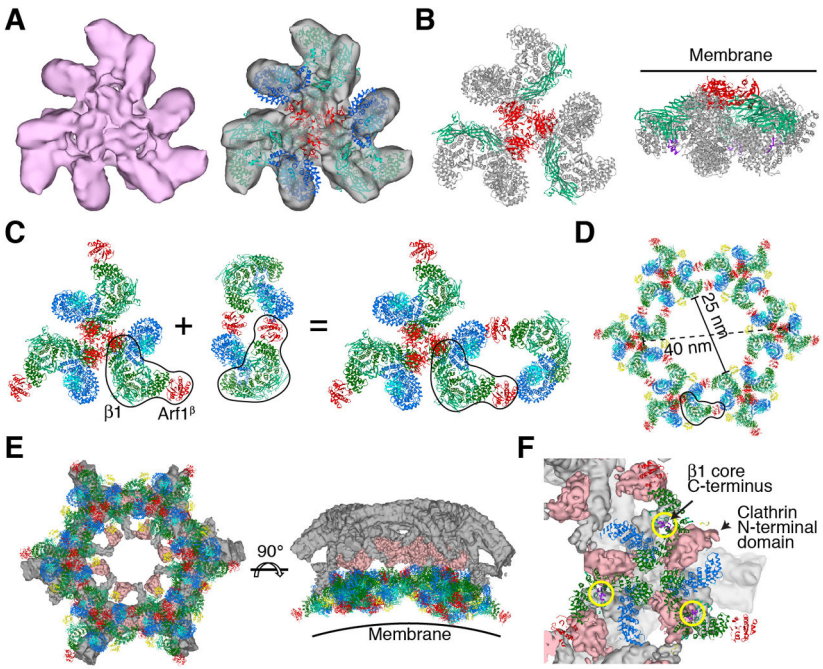

Fig. 4.

The open AP-1:Arf1:tetherin-Nef trimer suggests a hexagonal assembly model. (**A**) Reconstruction and docking of the open AP-1:Arf1:tetherin-Nef trimer. (**B**) The open AP-1:Arf1:tetherin-Nef trimer. The reported membrane and cargo binding subunits including Arf1, μ1 and Nef are kept in their original colors, while the other parts are colored grey. The membrane is represented by a line. The C-terminus of the β1 core, which is the location of the clathrin binding region, is colored purple. (**C**) The open AP-1:Arf1 trimer formed in the presence of Nef (left) and the known Nef-free AP-1:Arf1 dimer (to the right of the plus sign) (9) were docked onto one another by overlaying one copy each of the β1 subunit and $Arf1^{\beta}$ (outlined in black) to yield the composite structure at far right. (**D**) Iterating the docking operation shown in (C) generates the hexagon shown. Nef was docked onto all copies of AP-1 in the mode identified in the closed trimer, and is shown in yellow. (**E**) Juxtaposition of the modeled hexagon and one hexagonal segment of the cryoEM reconstruction of the clathrin D6-barrel (29). The membrane binding face is represented by a curved line. (**F**) A close-up of the hexagon model and the clathrin D6-barrel density shows that the clathrin binding site on β1 adjoins the AP-1 binding site on clathrin.

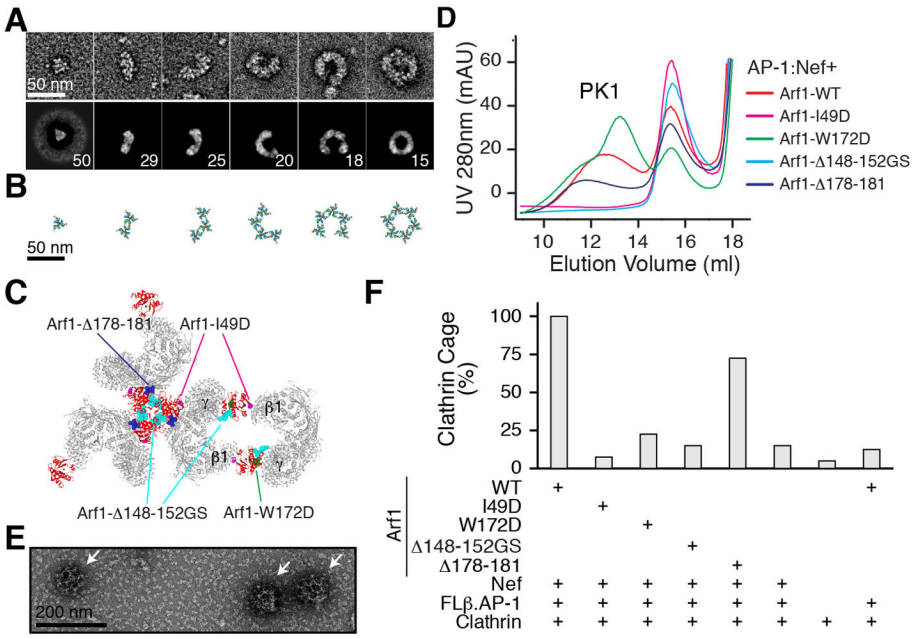

Fig. 5.

Visualization and validation of AP-1 polygons. (**A**) Negative stain EM of the high molecular weight tail of the size exclusion separation of AP-1:Arf1:MHC-I-Nef. The top row shows representative particles. The second row shows 2D class averages, which were carried out to quantitate the relative frequency of different assemblies. The number of particles within each class is indicated. The class averages show blurring and loss of density at the edges, indicative of heterogeneity within the classes. (**B**) The corresponding docked model. The scale is as same as in (A), indicating good agreement with the single particle images. (**C**) Location of Arf1 mutants in interfaces. Arf1 is red, while the other parts are colored grey. (**D**) Size exclusion chromatography of AP-1:Arf1:Nef mixtures, showing that Arf1 mutants interfere with dimerization or trimerization of AP-1. In $Arf1^{\Delta 148\text{-}152GS}$, residues $L_{148}RHRN_{152}$ were replaced by AGSGS. (**E**) Negative stain EM of clathrin cages assembled in vitro from purified clathrin, AP-1 core including full-length β1 ("FLβ.AP-1", following terminology used for AP-2 (38)), wild-type Arf1, Nef, and the non-hydrolyzable GTP analogue GppCp. (**F**) The relative percentage of clathrin cages were counted in 22 randomly chosen fields of view for the indicated mixtures of wild-type and/or mutant Arf1 proteins.

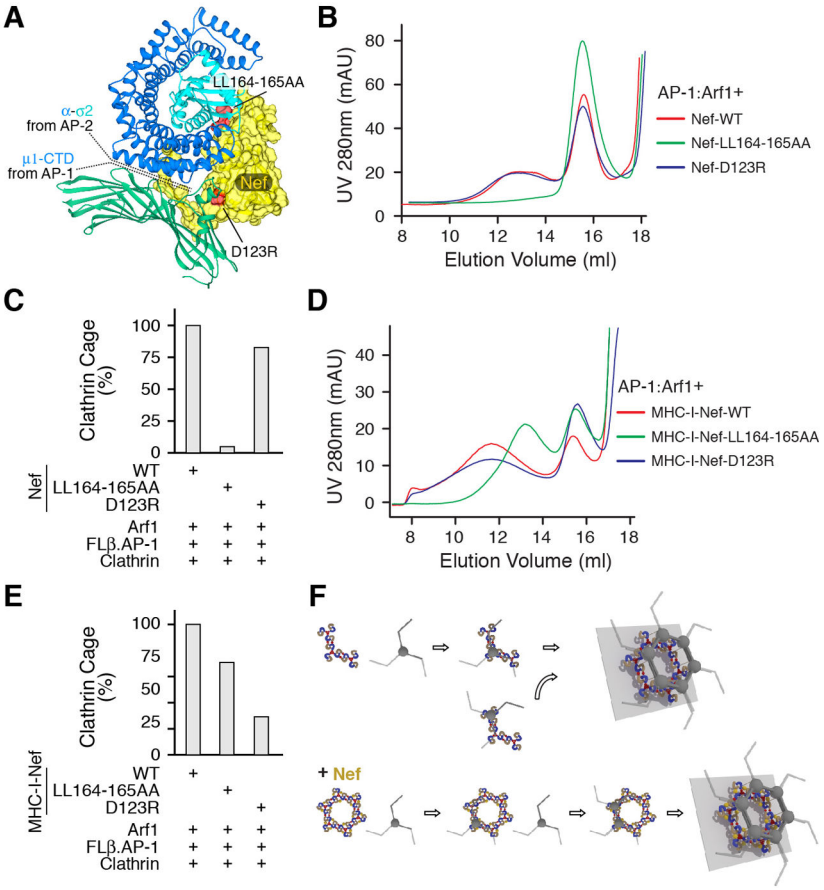

Fig. 6.

The hexagonal inner coat promotes clathrin cage assembly. (**A**) Diagram of Nef mutants. Structures from AP-2-α-σ2:Nef (PDB ID 4NEE) and AP-1-μ1:MHC-I-Nef (PDB ID 4EMZ) were combined and homologs are colored as before. (**B**) Size exclusion chromatography of AP-1:Arf1:Nef mixtures, showing that Nef mutants interfere with dimerization or trimerization of AP-1. (**C**) The relative percentage of clathrin cages were counted in 20 randomly chosen fields of view for the indicated mixtures of wild-type and/or mutant Nef proteins. (**D**) Size exclusion chromatography of AP-1:Arf1:MHC-I-Nef mixtures, showing that MHC-I-Nef mutants interfere with dimerization or trimerization of AP-1. (**E**) The relative percentage of clathrin cages were counted in 20 randomly chosen fields of view for the indicated mixtures of wild-type and/or mutant MHC-I-Nef proteins. (**F**) Concept for the role of AP-1:Arf1 polygons in clathrin assembly with Nef. Nef (yellow) stabilizes the AP-1:Arf1 polygons increases such that closed polygons can form even without clathrin, creating a pre-formed template for rapid clathrin assembly.